

The Structure and Growth Rates of
 $\text{Ge}_7\text{Sb}_{93}$ -Crystals

Bart-Jan Niebuur

January 22, 2013

Abstract

In this report, the properties of $\text{Ge}_7\text{Sb}_{93}$ -crystals, which are related to the use of this material in nonvolatile data storage devices, have been investigated. These Sb-rich phase change materials were in the past found to show highest possible growth speed, but turned out to have some problems with phase stability. A detailed study about the material might reveal new insights which can be useful in this area of research. The internal structure as well as the growth rate at certain temperatures of $\text{Ge}_7\text{Sb}_{93}$ -crystals have been investigated. A transmission electron microscope is used to investigate the samples, consisting of a 50nm thick $\text{Ge}_7\text{Sb}_{93}$ -layer on a silicon-nitride substrate. Diffraction is used to investigate the internal structure of the crystals while in-situ heating is used to measure the growth rate of the material at various temperatures. Also a heating stage in combination with an optical microscope is used to measure the growth rate as a function of temperature. Crystals with an overall triangular shape were observed, where in the centers of these crystals the hexagonal lattice is aligned vertical, hence with the c-axis pointing upwards. In the direction of the corners, the lattice rotates in the direction of that corner and grows eventually at a constant angle of 53° with respect to the lattice in the center. The relation between the growth rate of the crystals and the temperature is found to be of Arrhenius type with an activation energy for growth of about 2.2 eV.

Contents

1	Introduction	2
2	Basic principles	3
2.1	Phase-change materials	3
2.2	Phase-change recording properties	3
2.3	Germanium-Antimony	4
2.4	Transmission Electron Microscopy (TEM)	6
2.5	Diffraction	7
3	The structure of Ge₇Sb₉₃ crystals	10
3.1	Experimental procedure	10
3.2	Sample preparation	10
3.3	Orientation of the crystal-center	10
3.4	Orientation of the crystal-corners	14
3.5	Direction of the structure rotation	17
3.6	Orientation between the center and the corners of the crystal	22
3.7	Conclusions	24
4	Crystal growth front speed	26
4.1	Experimental procedure	26
4.2	Results	26
4.3	Activation energy	28
4.4	Possible side effects	30
4.5	Influence of the electron beam	32
4.6	Influence of preheating the material	33
4.7	Influence of location on the sample	35
4.8	Differences in heating the material	36
4.9	Conclusions	37
5	Acknowledgments	39
6	Appendices	41
6.1	All measured growth rates	41
6.2	Vegard's law	42
6.3	Vectors in the Miller-Bravais index system	43

Chapter 1. Introduction

Devices for data storage and (digital) recording were in the past and are still an important topic of research. Three materials-properties that in the recent history have been used to store data are magnetism, optical reflectivity and electrical properties. In some specific cases where devices use optical reflectivity or electrical resistivity, data can be stored and erased due to amorphization and crystallization of small pieces of material inside the device. An important field in this research is finding materials which can be used to increase the writing speed, the archive stability and the endurance for the recording device. To cause crystallization, the pieces are heated with a laser in case of an optical recording device and with a strong electrical pulse in case of an electrical recording device. At a certain temperature, the crystallization speed should be as high as possible. To prevent losing data, the crystallization speed of the recording material should be as low as possible at room temperature and for temperatures up to about 100°C. Besides a high crystallization speed, the contrast between the amorphous and crystalline phase is important. To read the information, the device must be able to distinguish amorphous from crystallized material.

Materials used and still considered best for this purpose are usually a composition of germanium, antimony and tellurium. For a long time it was assumed that $\text{Ge}_2\text{Sb}_2\text{Te}_5$ is the most optimal composition, considering the various requirements including crystallization speed and contrast for these so-called phase-change materials [1]. However, there are still many alternative competing compositions and not every composition has been investigated already. This report focuses on the composition containing 7 atomic percent germanium and 93 atomic percent antimony, $\text{Ge}_7\text{Sb}_{93}$. Earlier work done by Philips showed that these Sb-rich alloys showed the highest crystallization rates ever found for phase-change materials with speeds up to 50 m/s [2] [3]. However, a strong disadvantage of these Sb-rich alloys are their strong driving force for decomposition, i.e. phase separation limiting the cyclability of these materials. In the present work the crystallization speeds of this material is studied at different relatively low temperatures, which particularly provide an estimate of the data retention, but does not provide information of the maximum crystallization speed. A very important part of the present work is that the structure of the crystals grown will also be studied in detail with transmission electron microscopy.

Chapter 2. Basic principles

2.1 Phase-change materials

A phase-change material is a material that can adopt at least two states with different properties, with a reversible phase transformation providing access to the two (or multiple) states. The specific state is generally fixed for a certain temperature and pressure. For example, water possesses a fluid state at room temperature and with a pressure of 1 atm. The state becomes vaporized when the water is heated.

An example which is more interesting for this research, is the difference in crystalline and amorphous structures for certain solid materials. Quickly cooling such a material for instance from the liquid state will ensure that there is not enough time to crystallize the material. This material will become amorphous. The crystalline and amorphous state will for certain materials show pronounced differences in for example optical reflectivity and electrical resistivity.

The transition between the amorphous and crystalline state can occur in several ways. Possibilities are nucleation-dominant and growth-dominant crystallization. With the former type of crystallization, the crystal starts to grow from several points inside the amorphous area while with the latter type crystallization, the crystal grows only from the boundary of the amorphous region. Usually, a material crystallizes in both ways at the same time where one of the two ways is the dominant one [4].

2.2 Phase-change recording properties

The differences in optical reflectivity or electrical resistivity of different states of materials are used in designing recording devices. A recording device can consist of a lot of small pieces of phase-change material. Each piece can be controlled separately. When no data is stored, the complete set of material pieces must be in crystalline state. Every piece represents a 0. Data is stored by changing some pieces in amorphous material where every amorphous piece represents a 1. This phenomenon with switching between relatively stable amorphous and crystalline states is called the Ovonic memory switching (OMS) [5].

By measuring the electrical resistivity or optical contrast, it is possible to determine the state of the material. This measuring is usually done by applying

a tiny current or a low intensity laser pulse. In case of the current, it has to be tiny because the material must stay at a low temperature. The same thing holds for the laser. The temperature must stay low to avoid changes in the material. If a piece must change from the crystalline state to the amorphous state, a very short, high energetic pulse is applied. This will result in melting and quickly cooling of the material. As mentioned before, an amorphous state is reached. A change from the amorphous state to the crystalline state is achieved by applying a relatively long, moderately energetic pulse on the material. Hence, the temperature will be above the glass transition temperature, but below the melting temperature and there will be enough time to recrystallize the material [4].

The phase-change material used in recording devices must fulfill some requirements. It is important that writing and erasing can be done very quickly. In other words, the crystals must grow with very high speeds. At the other hand, the data must be preserved for a long time at room temperature, i.e. the crystals must grow very slow. To investigate the usefulness of a material, one has to find the growth rates at different temperatures. Since growth rates are usually too low to measure at room temperature, one has to extrapolate the results at higher temperatures to find the data retention.

Another important property which a potential recording-material must satisfy is measurable differences in properties between the crystalline and amorphous phase. Depending on the type of device used, a material must have different electrical resistivity or optical contrast for both phases. After trying metals, chalcogenides (chemical compounds with at least one atom from the oxygen family), particularly the ones containing Te, were considered the most promising materials for optical memory-devices due to their optical properties. Recent research focuses on finding chalcogenides with high crystallization rates [5]. However, apart from chalcogenides also Sb is considered a very important element of phase-change materials. Alloys only containing Te and/or Sb have amorphous phases that are not sufficiently stable at temperature of 100°C or lower. Therefore additional elements like Ge, Ag or In are required to stabilize the amorphous phase sufficiently at these low temperatures. All the requirements seem to be best fulfilled by alloys containing Ge, Sb and Te.

The overwrite cyclability of the recording material is also of great importance. Writing and erasing will eventually result in loss of quality of the recording device. Some causes are changes in thickness of the material, diffusion from layers or air adjacent to the recording material and defects caused by thermal stresses [4]. Change in thickness of the material can be avoided by strengthening the material. This can be done by adding dopants with a melting temperature higher than the phase-change material. The doping will remain in a solid state at higher temperatures and will therefore protect the phase-change material.

2.3 Germanium-Antimony

The properties of the germanium-antimony system are advantageous for recording applications. There is a good contrast between the crystalline and amor-

phous state and the crystallization speed is high. The crystallization speed depends on the amount of germanium in the system. Figure 2.1 shows the crystallization speed as a function of temperature for $\text{Ge}_6\text{Sb}_{94}$, $\text{Ge}_7\text{Sb}_{93}$, $\text{Ge}_8\text{Sb}_{92}$ and $\text{Ge}_9\text{Sb}_{91}$ [6]. As can be seen in figure 2.1, the straight line fits to the data in the Arrhenius plot become steeper with an increasing amount of germanium. Steeper lines means a higher crystallization rate at high temperatures and lower crystallization rates at low temperatures. As a consequence, writing can be done very fast at high temperature and information will preserved for a long time at low temperatures.

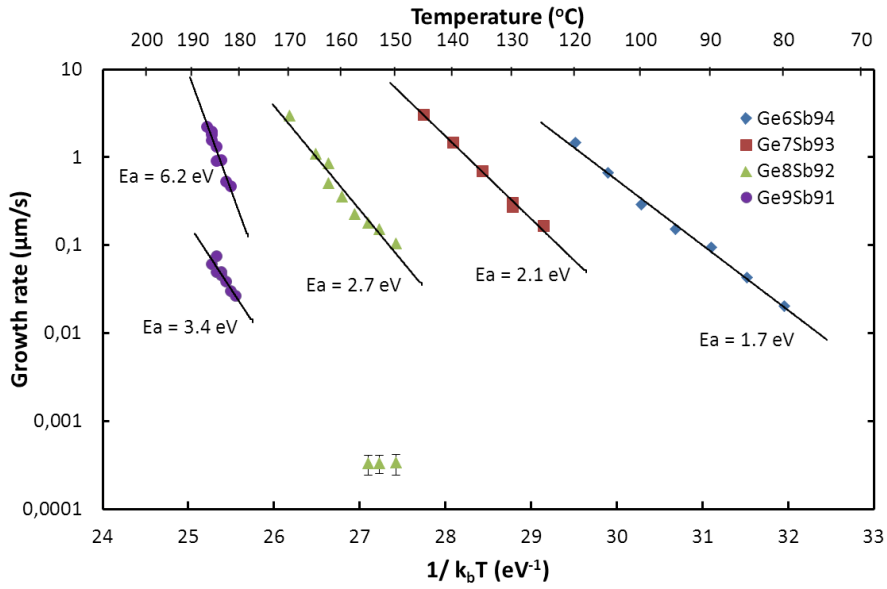


Figure 2.1: Growth rate as a function of temperature.

With small amounts of germanium, the system will have the same hexagonal crystal structure as pure antimony with germanium atoms substituting on antimony sites [7]. Pure antimony structure adopts a rhombohedral lattice with space group $R\bar{3}m$: trigonal lattice with all three axes of equal length, $a=b=c$, and the three possible angles between all axes of equal value, $\alpha=\beta=\gamma$. In case of antimony, the length of the axes is 4.506 \AA and the angles between the axes is 57.1° . As shown in figure 2.2, rhombohedral lattice is a specific type of hexagonal lattice. The lattice parameters of the structure of pure antimony in hexagonal form equals $a = 4.307 \text{ \AA}$ and $c = 11.273 \text{ \AA}$. This type of hexagonal structure is similar to the FCC structure (in fact Sb has resemblance to a distorted NaCl structure). However, the ratio c/a in case of FCC structure is ideal, i.e. the factor c/a is such that the atomic packing factor is maximum. Germanium and antimony do not have the same atomic radius. Therefore, the lattice parameters of the GeSb lattice will differ from the pure antimony lat-

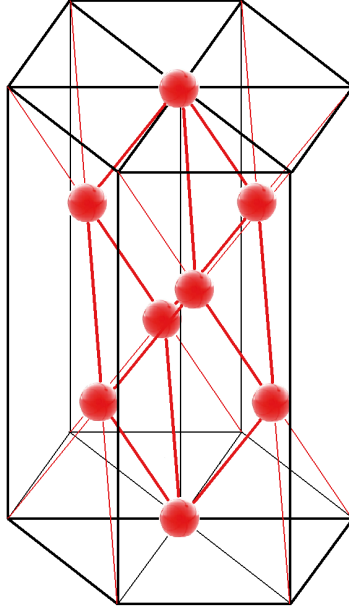


Figure 2.2: The crystal structure of pure antimony given as rhombohedral and hexagonal lattice.

tice. It is determined for $\text{Ge}_{16.7}\text{Sb}_{83.3}$ that the a-axis of the hexagonal lattice is shrunken to 4.185 \AA and the c-axis is grown to 11.320 \AA compared to pure Sb lattice [8]. Linear interpolation to get the lattice parameters of $\text{Ge}_7\text{Sb}_{93}$ gives an a-axis of 4.256 \AA and a c-axis of 11.293 \AA , both differ roughly 0.2% from these values with pure Sb. It is likely that the lattice parameters are not linearly proportional to the percentage germanium inside the germanium-antimony system. However, this first order approximation is probably sufficient in this research.

2.4 Transmission Electron Microscopy (TEM)

An electron microscope is used when an experiment requires better spatial resolutions than an optical microscope can provide or when a larger depth of focus or depth of field is required. The maximum resolution of every microscope (under diffraction-limited conditions) is limited by the wavelength of the radiation used. The smallest distance that can be resolved is of the same order as the wavelength. Therefore, the resolution of an optical microscope is limited to several hundred nanometers. In case of electrons, the wavelength is approximately given by [9]

$$\lambda = \frac{1.22}{\sqrt{E}}, \quad (2.1)$$

with λ given in nanometers and E given in electron volts. For example, a 100-Kev electron microscope should be able to produce images with a resolution of several picometers. However, this ultimate resolution is not reached, because of aberrations (particularly spherical aberration) or stability issues (e.g. of high tension and lens currents) limit the resolution to 0.1-0.2 nm.

In a transmission electron microscope (TEM), the image of the sample is made by transmitted electrons. The electrons are released by an electron source. These electrons will gain speed due to the interaction with a potential-field. A set of electromagnetic lenses, the so-called condenser lenses, aligns and focuses the electron beam on the sample. The interaction with the sample will cause scattering of the electrons in the beam. In order to obtaining sufficient quality TEM images, elastic scattering should strongly dominate over inelastic scattering. Another set of lenses (including objective, intermediate and projector lenses) will use the non-scattered and scattered (including diffracted) electron beams after the sample to make a magnified image of the sample. By switching the strength of the intermediate lens it is possible to switch between the imaging and diffraction mode in the TEM.

In order to make it possible for the electron beam to show sufficient transmittance through the sample, it has to be very thin, even in case of accelerating voltages of a few hundred KeV. Dependent of the used electron energy, the sample cannot be thicker than about 100 nm to produce a discernible image. Due to this limited thickness, the specimen is usually too weak to be a self-supporting specimen. In that case, the sample of the to be investigated material can be supported on a specimen support grid. In other cases, volumes are only removed in specific regions of the sample such that this transparent wedges near a hole or thin transparent windows with limited dimensions remain.

2.5 Diffraction

Diffraction patterns can be used to provide information about the structure of the investigated material. Several devices are able to produce such patterns, including the TEM. The advantage of TEM is that imaging and diffraction can be combined, such that the diffraction pattern originates from a selected area of the imaged sample. With electron diffraction in the TEM, diffraction can be performed on much smaller volumes than with e.g. X-ray diffraction. A material composed of crystals of a few nanometers can appear amorphous in X-ray diffraction, but with TEM such crystalline diffraction patterns can still be recorded.

The incident beam is due to scattering by the atoms in the crystal diffracted in various beams. With constructive interference, spots on the screen are formed corresponding to the Bragg-diffracted beams. These spots thus represent diffraction on sets of planes in the crystal and can be defined by a reciprocal lattice vector \vec{G} . Figure 2.3 gives a visualization of this concept. With trigonometry from figure 2.3, it can be determined that the relation between the angle between the direct beam and the diffracted beam and the distance R between the

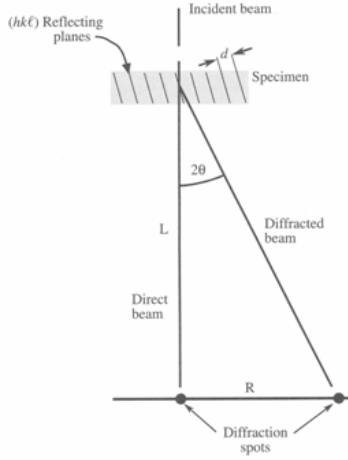


Figure 2.3: A visual explanation about diffraction pattern production.

central diffraction spot and the spot caused by the diffracted beam equals

$$\tan(2\theta) = \frac{R}{L}. \quad (2.2)$$

Because θ is generally not more than 1-2 degrees, $\tan(2\theta)$ can be approximated by

$$\tan(2\theta) \approx 2\sin(\theta). \quad (2.3)$$

With help of Bragg's law,

$$2d * \sin(\theta) = \lambda, \quad (2.4)$$

the relation between the distance between the diffraction spots and the actual distance between the represented planes is found to be

$$d = \frac{L\lambda}{R}. \quad (2.5)$$

The measuring equipment calibrates the scales so that the formula

$$d_{hkl} = \frac{1}{|\vec{G}|} \quad (2.6)$$

can be used to determine distance, or d-spacing, between planes from the lattice vector \vec{G} , the distance between the diffraction spots in the created diffraction pattern [9]. When producing diffraction patterns with the TEM, only planes with a normal vector perpendicular, or almost perpendicular, to the electron beam are visible.

Electron diffraction patterns as recorded with the TEM contain two basic types of information. The spatial arrangements of the visible dots give information

about the distances and angles between planes in the crystal(s) as defined by various reciprocal lattice vectors \vec{G} ; distances between diffraction spots (or less common diffraction rings) can be easily related to inter planar spacings as indicated by equation 2.6. Besides that, intensities in the diffraction pattern gives information about the scattering of the repeating structural unit, i.e. about the type and number of atoms present. Very difficult to predict intensities, due to dynamical diffraction, generally require computer assistance.

Chapter 3. The structure of $\text{Ge}_7\text{Sb}_{93}$ crystals

3.1 Experimental procedure

In this section, results of the TEM analysis of $\text{Ge}_7\text{Sb}_{93}$ -crystals are presented to study the way they grow. Diffraction will be used to investigate the structure of different parts of the crystals. For this research, a $\text{Ge}_7\text{Sb}_{93}$ -layer with a thickness of 50 nm on a silicon-nitride substrate is used. Because the sample consists of completely amorphous $\text{Ge}_7\text{Sb}_{93}$, it will be partly crystallized before the TEM is used.

3.2 Sample preparation

The $\text{Ge}_7\text{Sb}_{93}$ -samples are partially crystallized with a heating device which is capable of heating at precise temperatures. In the sample, the $\text{Ge}_7\text{Sb}_{93}$ film is supported by a silicon nitride substrate. In fact, the support is a piece of Si wafer with a thin amorphous Si-nitride film (20 nm thick) on one side where on certain parts the Si has been etched away such that thin transparent Si-nitride windows remain which allow TEM analysis. The TEM-windows have sides with a length of 100 μm . Only these parts of the sample are useful for transmission electron microscopy and should be partly provided with crystals. In order to reach controllable crystal growth, the temperature for crystallizing $\text{Ge}_7\text{Sb}_{93}$ has to be around 130° according to figure 2.1. An optical microscope is used to check the progress of the growth. Figure 3.1 shows a part of a sample which is prepared for the electron microscopy experiments. As can be seen, the crystals grow in a triangular shape. The TEM-windows are not visible on this image. It is therefore not possible to see if crystals are grown in these areas. Fortunately, there are some crystals found with the TEM.

3.3 Orientation of the crystal-center

Figure 3.2 shows the TEM-image of a crystal found on the partially crystallized $\text{Ge}_7\text{Sb}_{93}$ -sample as well as the diffraction patterns taken in the center of the

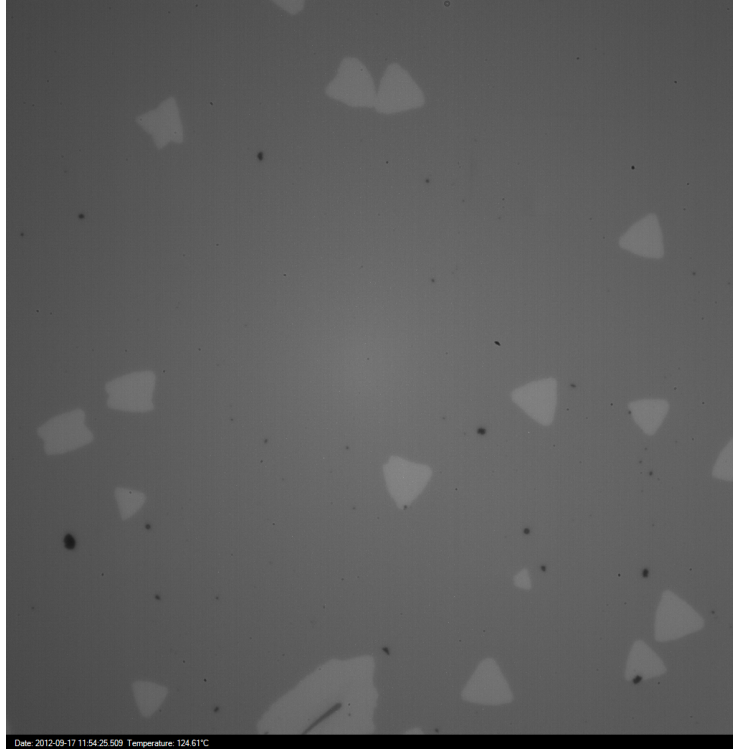


Figure 3.1: Partially crystallized $\text{Ge}_7\text{Sb}_{93}$ -sample, zoomed in 100 times.

crystal and at each corner. As can be seen in the image, the diffraction pattern at the center, denoted with the 1, consist of a very bright hexagon close to the central spot. This is clearly the representation of the most common sets of crystal planes perpendicular to the viewing direction of this area. The d-spacing between these planes can be calculated with equation 2.6. The absolute value of the G-vector is for each dot in the hexagon around 4.67 nm^{-1} . There is however a relatively large error possible. Depending on the alignment of the TEM, this value can vary by 0.1 nm^{-1} . This absolute value of the G-vector corresponds with a d-spacing of $d_{hkl} = 2.15 \pm 0.05 \text{ \AA}$.

To find the corresponding plane, one can compare the value of the found d-spacing with known d-spacings from planes in the Sb-lattice. As said before, the Ge-atoms replacing Sb-atoms in the hexagonal structure of the combined GeSb-system change the lattice parameters. This will also affects the d-spacings between planes in the lattice. The distances between planes which are oriented perpendicular to the c-axis in $\text{Ge}_7\text{Sb}_{93}$ -lattice are bigger compared to the same planes in pure antimony while the distance between planes which are oriented parallel to the c-axis in $\text{Ge}_7\text{Sb}_{93}$ -lattice are smaller compared to the same planes in pure antimony. This implies that planes with a small a_4 -index in the Miller-Bravais index system will have a smaller d-spacing in $\text{Ge}_7\text{Sb}_{93}$ -lattice than in

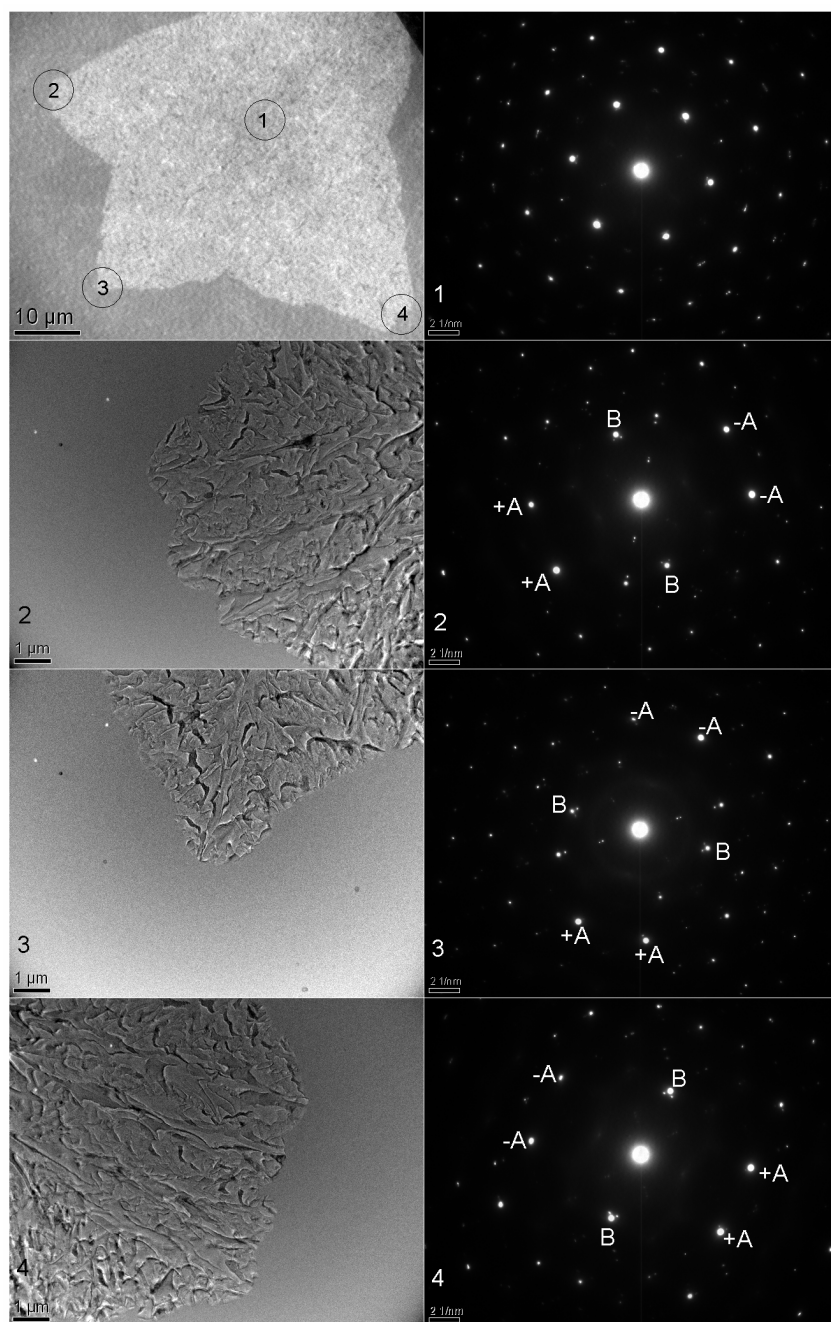


Figure 3.2: Overview of a crystal and diffraction patterns.

pure Sb-lattice and vice versa.

According to information from the International Center for Diffraction Data, a possible match for the found d-spacing is the distance of 2.152 Å corresponding to the (110)-plane, or (11 $\bar{2}$ 0) in the Miller-Bravais index system. Because this plane is aligned parallel to the c-axis of the hexagonal lattice, the d-spacing between this planes in pure Sb-lattice should be slightly bigger than in Ge₇Sb₉₃-lattice, which is indeed the case here.

Figure 3.3 shows a possible indexing of the hexagonal from figure 3.2. To ver-

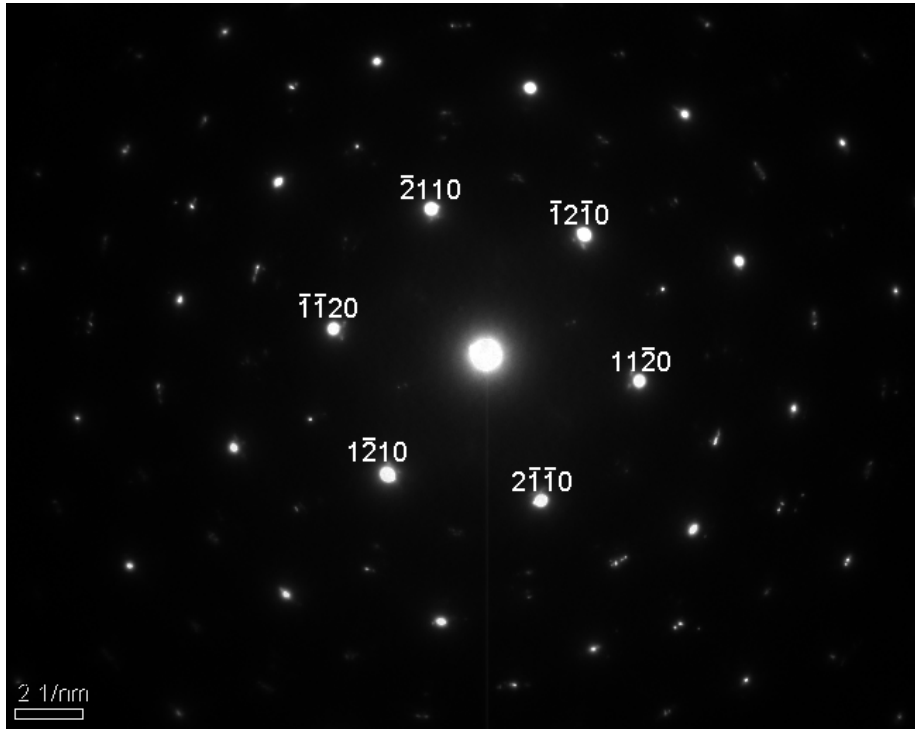


Figure 3.3: Possible indexing of the diffraction pattern in the center of the crystal.

ify the correctness of the (11 $\bar{2}$ 0)-plane, the angle between two planes in the diffraction pattern and in real space can be compared. It is clear from figure 3.3 that the angle is 60° between for instance the (11 $\bar{2}$ 0)- and the ($\bar{1}$ 2 $\bar{1}$ 0)-plane. Figure 3.4 shows the (11 $\bar{2}$ 0)- and ($\bar{1}$ 2 $\bar{1}$ 0)-plane in the hexagonal structure of Sb-lattice. The direction-dependency of d-spacing differences between planes in Ge₇Sb₉₃ and pure Sb imply that the angle between two planes in the Ge₇Sb₉₃-lattice differs from the angle between the same two planes in pure Sb-lattice. however, because the changes in lattice parameters are only about 0.2%, the difference in the angle between planes in Ge₇Sb₉₃ and pure Sb is negligible. The angle between the two planes shown in figure 3.4 can be calculated by determining the normal-vectors of both planes. It can easily be seen that the

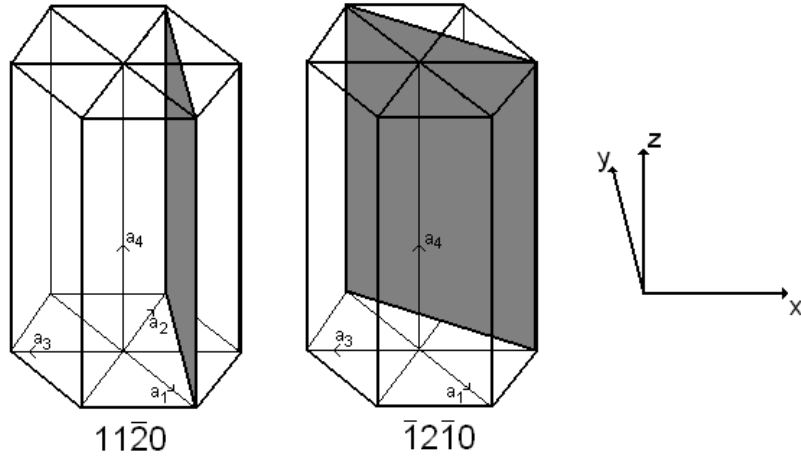


Figure 3.4: $(11\bar{2}0)$ and $(\bar{1}\bar{2}10)$ -plane drawn in the hexagonal structure.

normal-vector of the $(11\bar{2}0)$ -plane equals $\vec{n}_{11\bar{2}0} = \hat{x}$. The normal-vector of the $(\bar{1}\bar{2}10)$ -plane lies in the a_2 -direction according to figure 3.4. The angle between the x - and a_2 -direction is by definition 60° . The angle between the two planes is therefore also 60° . Since this angle corresponds with the angle found in the diffraction pattern, it is proven that the bright spots from the hexagonal in the diffraction pattern all represent possible members of the $(11\bar{2}0)$ -plane family.

As said before, only planes with a normal vector perpendicular to the electron beam are visible in the diffraction pattern. The orientation of the crystals can therefore be found by finding the direction of the electron beam, \vec{B} , relative to the crystal. The dot product between the normal vector of each plane found and the direction of the electron beam should be zero to satisfy this requirement:

$$(11\bar{2}0) \cdot \vec{B} = 0 \quad (3.1)$$

or the dot product of the normal-vector of each other member of the $(11\bar{2}0)$ -family with \vec{B} . The only possibility to satisfy this equations is an electron beam direction of $[0001]$ relative to the crystal. The crystal is therefore standing upright, or, the orientation of the a_4 -axis is aligned vertical.

3.4 Orientation of the crystal-corners

The orientation of the lattice at the corners of the crystals is determined at exactly the same way as the orientation of the lattice at the center. In figure 3.2 the diffraction patterns from each corner of the crystal are given. All three diffraction patterns of the corners are in fact the same. The only difference is that they are rotated with respect to each other by 120° around the same

viewing direction, i.e. normal to the plane with diffraction spots. In every diffraction pattern of the corners, it is visible that two bright spots (indicated with +A in the images) are located in the direction of the tip seen from the central spot and two other bright spots (indicated with -A) are located in the direction of the center of the crystal. Just between the two sets of two spots is another set of two bright spots (indicated with B) visible. Measurements on the G-vector of these last two spots show that they again represent members of the $(11\bar{2}0)$ -family. With the line between this spots perpendicular to the growth-direction, it shows that the only rotation occurred with respect to the crystal structure in the center of the crystal is around the in-plane axis perpendicular to the growth-direction.

To determine the amount of rotation, i.e. the angle between the orientation of the lattice at the corners relative to the lattice in the center, the four other bright spots from the diffraction patterns in the corners are helpful. The distance from the central bright spot to each of the four spots equals $7.32 \pm 0.1 \text{ nm}^{-1}$. According to equation 2.6, this is equal to a d-spacing of $d_{hkl} = 1.36 \pm 0.05 \text{ \AA}$. The closest match for this distance is the $(11\bar{2}6)$ -plane with a d-spacing of 1.416 \AA . A possible indexing for the diffraction pattern of the left corner, number

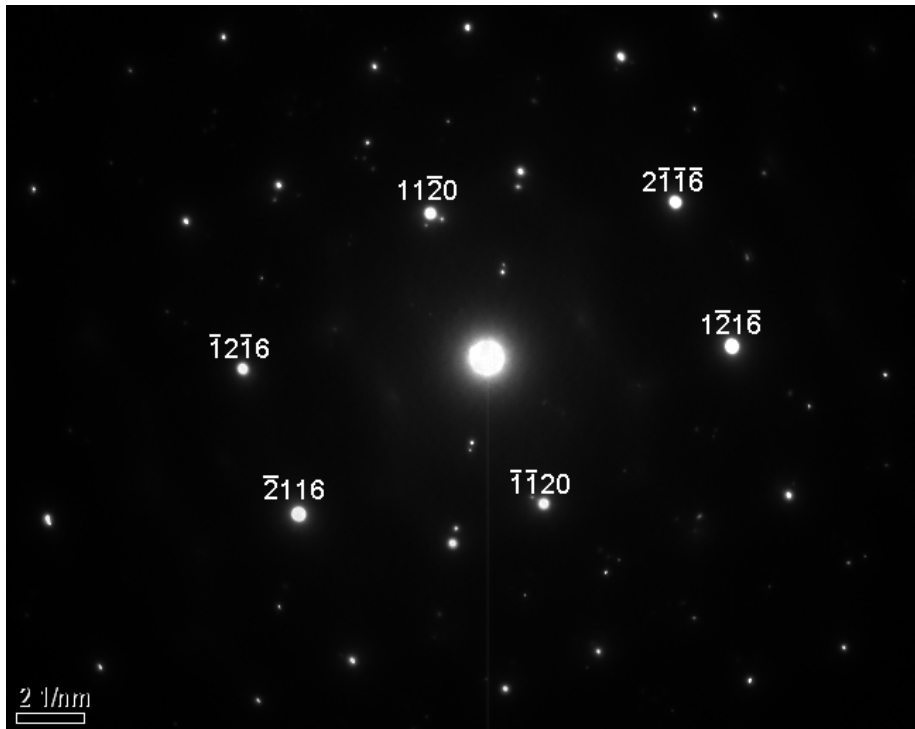


Figure 3.5: diffraction pattern of the left corner (indicated with 2 in figure 3.2) with indexing.

2 in figure 3.2, is shown in figure 3.5. To prove that the $(11\bar{2}6)$ -plane is the

actual plane from the diffraction pattern, the angle between two planes is again determined. For instance, the angle between the $(\bar{1}2\bar{1}6)$ -plane and the $(11\bar{2}0)$ -plane in the diffraction pattern is $71 \pm 1^\circ$. The angle between these planes should give the same value in real space. Figure 3.6 shows both the planes drawn in the crystal structure. In this image, the normal vector of the $(11\bar{2}0)$ -

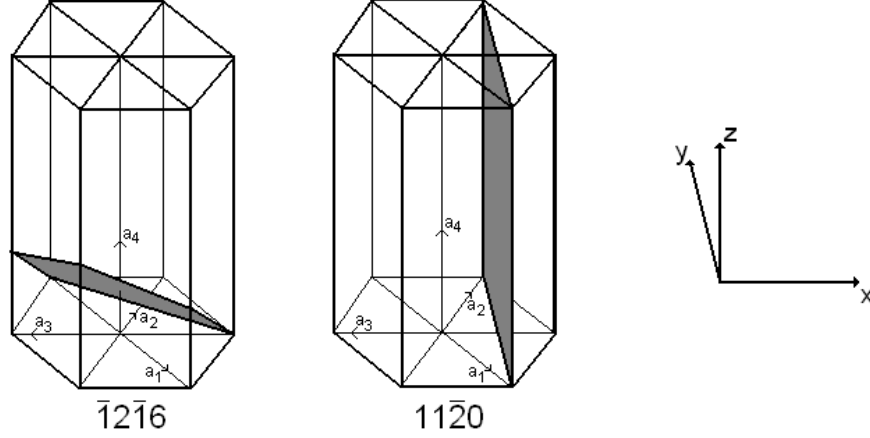


Figure 3.6: $(\bar{1}2\bar{1}6)$ and $(11\bar{2}0)$ -plane drawn in the hexagonal structure.

plane equals $\vec{n}_{11\bar{2}0} = \hat{x}$. The normal vector of the $(\bar{1}2\bar{1}6)$ -plane is more difficult to derive. With basic geometry, it is easy to see that three points defining this plane are

$$(A, B, C) = (a\hat{x}, -\frac{1}{2}a\hat{x} + \sqrt{a^2 - \frac{1}{4}a^2\hat{y}}, \frac{1}{6}c\hat{z}) \quad (3.2)$$

in the cartesian coordinate system. With this three points, the normal-vector of the plane can be calculated in the following way:

$$\vec{n}_{\bar{1}2\bar{1}6} = (B - A) \times (C - A). \quad (3.3)$$

With

$$(B - A) = -\frac{3}{2}a\hat{x} + \sqrt{a^2 - \frac{1}{4}a^2\hat{y}} \quad (3.4)$$

and

$$(C - A) = \frac{1}{6}c\hat{z} - a\hat{x}, \quad (3.5)$$

this gives

$$\vec{n}_{\bar{1}2\bar{1}6} = \begin{vmatrix} \hat{x} & \hat{y} & \hat{z} \\ -6.461 & 3.730 & 0 \\ -4.307 & 0 & 1.879 \end{vmatrix} = 7.008\hat{x} + 12.138\hat{y} + 16.065\hat{z} \quad (3.6)$$

with entered values for the lattice parameters a and c . The actual angle between the $(\bar{1}2\bar{1}6)$ -plane and the $(11\bar{2}0)$ -plane can be calculated with the dot product of the normal-vectors of both planes in the following way:

$$\theta = \cos^{-1}\left(\frac{\vec{n}_{11\bar{2}0} \cdot \vec{n}_{\bar{1}2\bar{1}6}}{|\vec{n}_{11\bar{2}0}| |\vec{n}_{\bar{1}2\bar{1}6}|}\right) = 70.81^\circ. \quad (3.7)$$

This value falls within the error margin of the angle calculated from the diffraction pattern. Therefore, it is likely that the investigated spots are part of the $(11\bar{2}6)$ -family.

To find the orientation of the lattice at the corners of the growing crystal, the equations

$$(11\bar{2}0) \cdot \vec{B} = 0 \quad (3.8)$$

and

$$(\bar{1}2\bar{1}6) \cdot \vec{B} = 0, \quad (3.9)$$

or the dot product of the normal-vector of each other members of both plane-families indicated in the figure 3.5 with \vec{B} , must be solved. The only possible value for \vec{B} to solve this system is $\vec{B} = [2\bar{2}01]$. This direction corresponds to an angle of 52.93° with respect to the c -axis of the hexagonal lattice, as determined in the way described in the appendix (chapter 6.3). Comparing the lattice orientation at the center and at the corners of the crystal, one can see that the lattice has rotated with an angle of 53° during the growth in such a way that the rotation axis is in plane and keeping one set of the possible three of the $(11\bar{2}0)$ -family present in the center of the crystal edge-on during rotation toward the corners, i.e. the rotation axis during growth is the normal of this one set of $(11\bar{2}0)$ -planes.

3.5 Direction of the structure rotation

From the previous calculations, it is impossible to see whether the rotation is positive or negative. A way to determine this is using the tilt-function of the TEM. In this way, the sample can be rotated by a certain angle. Due to the tilt, the angle of crystal at the corner with respect to the crystal at the center will be smaller or larger than 53° , dependent on the orientation of the crystal corner. With the change in orientation of the crystal center known, it can be calculated whether the underside or upper side of the crystal grows faster. Figure 3.7 shows an illustration of this idea. If the angle of the beam found in the tilted corner with respect to the c -axis is clearly bigger or smaller than 53° , one can make a statement about the orientation of the crystal structure in the corner.

In this case, the investigated crystal is oriented as shown in figure 3.7: the corner is located right of the center, as it is shown by the camera inside the TEM. It was hereby possible to see that negative tilt causes clockwise rotation of the center, as shown in figure 3.7. An diffraction pattern is again taken to determine

	Center	Corner	
If			with tilt = 0° ,
then			with tilt = -28.5° .
If			with tilt = 0° ,
then			with tilt = -28.5° .

Figure 3.7: The orientation of different crystal components for the two possibilities. With the direction of the beam vertical in this image, the angle of the crystal corner with respect to the electron beam with tilt depends on the orientation of the corner.

the orientation of the crystal corner with 28.5° tilt.

Figure 3.8B shows the diffraction pattern of the corner of the with 28.5° tilted crystal. The indexing is determined in exact the same way as before. The reciprocal distance between the spots in the diffraction and the central spot is compared to the distances of various planes in Sb-crystal found in literature. It is suspected that the spots denoted by a and a' are parts of the (116)-family, b and b' of the (214)-family and c and c' of the (122)-family. Because (116)-planes might be present, it is possible that the line between a and a' in the diffraction pattern is a representation of the tilt axis. This makes sense because members of the same plane-family are present at approximately the same position in the diffraction pattern of the corner without tilt, as can be seen in figure 3.8A.

A possible indexing consists of the $(3\bar{1}\bar{2}\bar{4})$ -plane at spot b, the $(1\bar{2}\bar{1}\bar{6})$ -plane at spot a and the $(\bar{2}\bar{1}\bar{3}\bar{2})$ -plane at spot c. The angles between all plane-representations in the diffraction pattern and between the same two planes in the real crystal are calculated and differ with a maximum value of 1° . To find the direction of the electron beam, $\vec{B}=[B_1 \ B_2 \ B_3 \ B_4]^T$, with respect to the specimen, the dot product of each indicated index with \vec{B} should produce zero. Besides that, \vec{B}

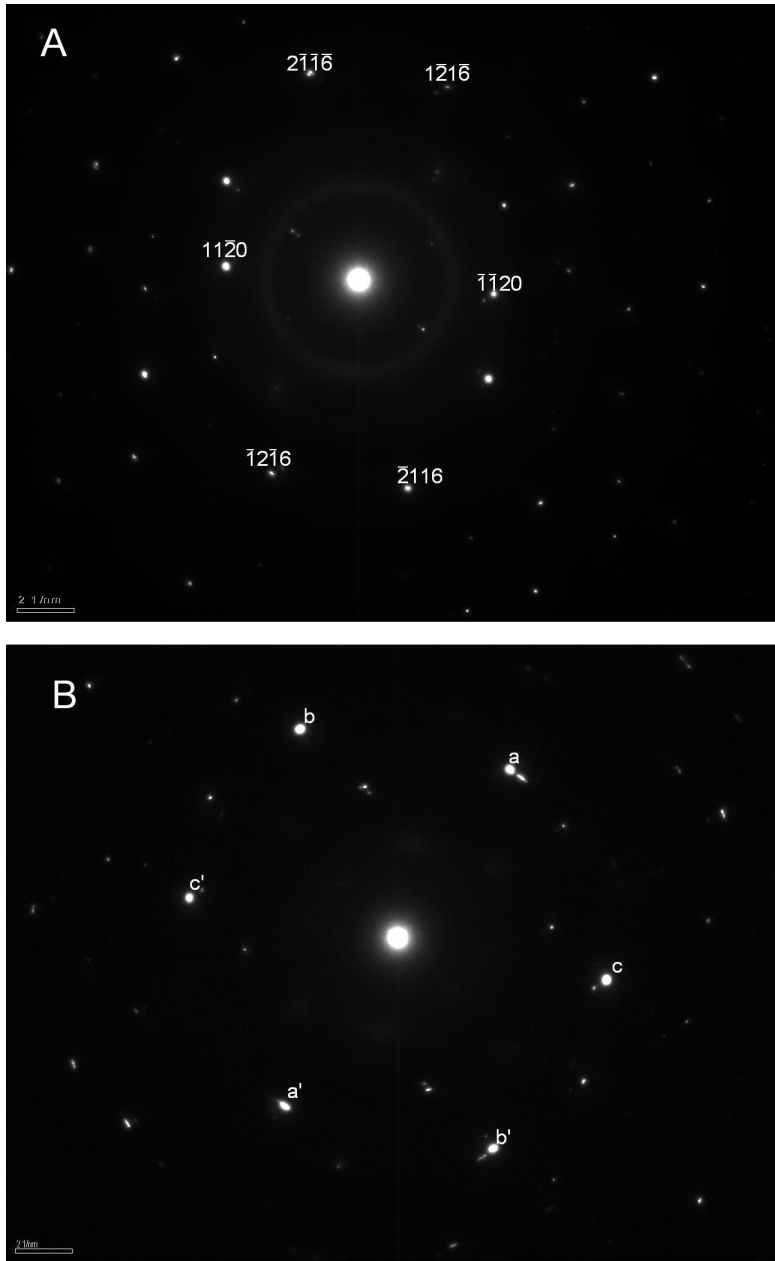


Figure 3.8: The diffraction pattern of the corner of a crystal without tilt (A) and with 28.5° tilt (B).

must follow the rules of the Miller-Bravais index system: $B_3 = -(B_1+B_2)$. The dot product of \vec{B} with the three given planes and the limitation imposed by the

Miller-Bravais index system can be collected in a system of equations:

$$\begin{aligned}
3B_1 - B_2 - 2B_3 - 4B_4 &= 0, \\
B_1 - 2B_2 + B_3 - 6B_4 &= 0, \\
-2B_1 - B_2 + 3B_3 - 2B_4 &= 0, \\
-B_1 - B_2 - B_3 + 0B_4 &= 0.
\end{aligned} \tag{3.10}$$

This system of equations can be converted to a matrix equation which is given by

$$\begin{pmatrix} 3 & -1 & -2 & -4 \\ 1 & -2 & 1 & -6 \\ -2 & -1 & 3 & -2 \\ -1 & -1 & -1 & 0 \end{pmatrix} \begin{pmatrix} B_1 \\ B_2 \\ B_3 \\ B_4 \end{pmatrix} = \begin{pmatrix} 0 \\ 0 \\ 0 \\ 0 \end{pmatrix}. \tag{3.11}$$

The reduced row-echelon form,

$$\begin{pmatrix} 1 & 0 & 0 & -1.2 \\ 0 & 1 & 0 & 2 \\ 0 & 0 & 1 & -0.8 \\ 0 & 0 & 0 & 0 \end{pmatrix} \begin{pmatrix} B_1 \\ B_2 \\ B_3 \\ B_4 \end{pmatrix} = \begin{pmatrix} 0 \\ 0 \\ 0 \\ 0 \end{pmatrix}, \tag{3.12}$$

is used to solve this system. The matrix equation from equation 3.12 can again be converted to a system of equations to find the components of \vec{B} :

$$\begin{aligned}
B_1 - 1.2B_4 &= 0, \\
B_2 + 2B_4 &= 0, \\
B_3 - 0.8B_4 &= 0,
\end{aligned} \tag{3.13}$$

$$\vec{B} = \begin{pmatrix} 1.2B_4 \\ -2B_4 \\ 0.8B_4 \\ B_4 \end{pmatrix} = \begin{pmatrix} 6 \\ -10 \\ 4 \\ 5 \end{pmatrix} \text{ with } B_4 = 5. \tag{3.14}$$

The direction of the electron beam with respect to the tilted specimen according to the given indexing equals $[6\bar{1}045]$. To verificate this direction, it should be compared with the direction of the beam at the corner of the non-tilted crystal, $[2\bar{2}01]$. The angle between these directions should give the same angle over which is tilted. By converting both vectors to vectors in the cartesian coordinate system, as described in the appendix (chapter 6.3), an angle of 18.56° is calculated. This value differs with 10° from the tilt angle of 28.5° . This difference is too large to approve the given indexing.

In order to find the correct indexing, all possible beam-directions related to the $[6\bar{1}045]$ -direction are compared with the $[2\bar{2}01]$ -direction. Both the $[4\bar{1}065]$ - and the $[10\bar{4}\bar{6}5]$ -direction are positioned with an angle of approximately 28.5° with respect to the $(2\bar{2}01)$ -direction. However, only the $[4\bar{1}065]$ -direction is capable of showing the $(1\bar{2}1\bar{6})$ -plane, as required. With help of this beam-direction, the correct indexing of the diffraction pattern given by figure 3.8B is designed and is given in figure 3.9.



Figure 3.9: The diffraction pattern of the corner of a crystal with 28.5° , correct indexing included.

The angle between the $[4\bar{1}065]$ - and $[0001]$ -direction equals 49.08° . This angle differs little from 52.93° , the angle between the structure in the corner of the untilted crystal and the center. This is a logical consequence of the tilt axis found in the diffraction patterns. Figure 3.8A and figure 3.9 show that the tilt axis is the line between the $(1\bar{2}1\bar{6})$ - and $(\bar{1}2\bar{2}6)$ -spot in both diffraction patterns. This line must be the tilt axis because both spots are present at approximately the same locations in both diffraction patterns. With the growth direction of the corner approximately vertical in this diffraction images, the tilt axis is almost parallel to the growth direction.

Therefore, this experiment is performed incorrectly. To be certain about the orientation with respect to the orientation at the crystal center, the found angle should have differed more from 52.93° . With the tilt axis perpendicular to the growth direction, the angle of the crystal in the corner would be more suitable for giving information about the orientation.

3.6 Orientation between the center and the corners of the crystal

In the previous sections, it is shown that the orientation of the lattice at the corners of the crystal differs with an angle of 53° from the center of the crystal. It might be interesting to see how this angle evolves from the center to the corners of the crystal. For this purpose, the diffraction pattern at different points at the crystal are investigated. Unfortunately, the TEM-window with the earlier investigated crystal broke during the preparation for the second TEM-session. A crystal on a different TEM-window is used for investigation of the evolving of the lattice-angle.

Somewhere halfway the distance between the center and the corners of the crystal, at a distance of around $7 \mu\text{m}$ from the center, the same diffraction patterns are found as the diffraction patterns on the corners. An overview of the crystal with the exact position where these diffraction patterns are taken is shown in figure 3.10. This implies, of course, that the angle of the lattice at this

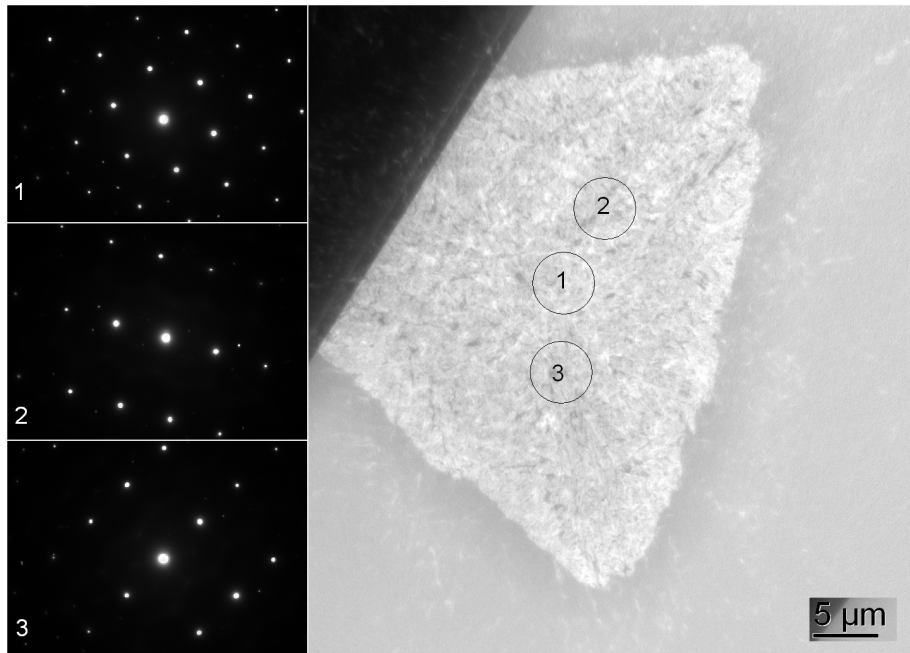


Figure 3.10: Overview of the crystal with diffraction patterns at the different points indicated.

points between the center and corners of the crystal are the same as the angle of the lattice at the corner. However this has to be proven further, it looks like the lattice grows at a constant angle from that certain distance from the center. Figure 3.11 shows the diffraction pattern of an area close to the center, before the angle of the lattice has reached a steady value. The blue arrow in the image

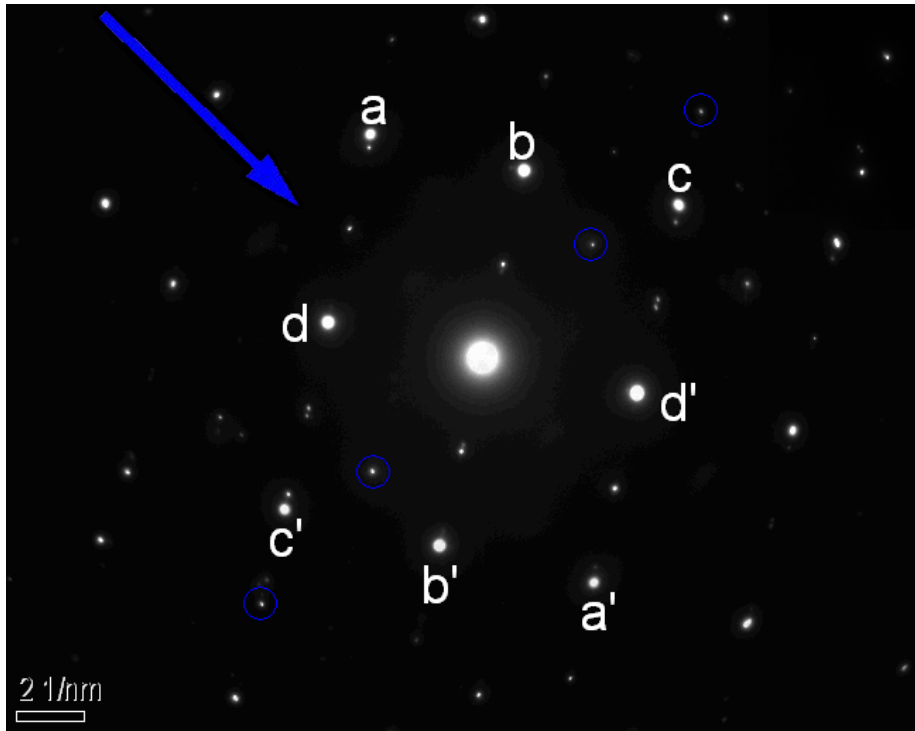


Figure 3.11: Diffraction pattern close to the center.

indicates the direction of the growth of the crystal. Exact perpendicular to the direction of the growth, representations of the (110)-plane are visible. These dots are indicated with the blue circles. It is clear that the given diffraction pattern contains at least two lattice-orientations: the recessive orientation containing the (110)-representations perpendicular to the growth direction and the dominant orientation represented by the bright spots indicated with a, b, c and d. A logical explanation is that the diffraction pattern is by mistake recorded just next to the line between the center and one of the corners of the crystal. The selected area for recording the diffraction pattern contained besides the part on which is focused also a small part of the line between the center of the crystal and one of the corners. This explains the presence of the (110)-representations perpendicular to the growth direction. Although it is impossible to find the orientation of the lattice on the line between the center and the corner closest to the selected area from this diffraction pattern, a statement can be made about how the orientation of the lattice evolves on the line from the center of the crystal to the corners. The diffraction pattern of figure 3.11 in combination with all other diffraction patterns in this report, shows that it is likely that on the complete length of the line between the crystal center and a crystal corner, the two (110)-representations perpendicular to the growth direction are present

in the diffraction pattern; this was already proven for the center of the crystal, somewhere halfway the crystal where the orientation has reached the steady value of 53° and at the corner of the crystal, but now also at some point close to the center of the crystal before the steady orientation is reached. The planes represented by the two spots which are aligned parallel to the growth direction, stays oriented edge-on during the growth of the crystal but rotates. Besides this rotation, no other change in the lattice orientation can occur between the center and the corners of the crystal.

As mentioned before, again the $(11\bar{2}0)$ -plane, indicated with the blue circles in figure 3.11, is found in the diffraction pattern. Also this time, these spots define the growth direction as in the direction of the closest corner. The spots indicated with d in figure 3.11 are also representations of the (110) -plane; the absolute value of \vec{G} is in accordance with the (110) -representations indicated with the blue circles and the difference in angle is 60° . According to figure 3.3, spot d should be indexed as $(\bar{2}110)$ and d' as $(2\bar{1}\bar{1}0)$.

The other points are more difficult to relate to a plane. Points a and c in figure 3.11 both define a plane with a d-spacing of $1.34 \pm 0.05 \text{ \AA}$ in, point b represents a plane with a d-spacing of $1.74 \pm 0.05 \text{ \AA}$. In the literature, a d-spacing of 1.770 \AA is found for the (202) -planes. This value is reasonable close to the value of $1.794 \pm 0.05 \text{ \AA}$ found for point b in the diffraction pattern. Because point b is oriented perpendicular to the $(2\bar{1}\bar{1}0)$ -plane in the diffraction pattern, $(02\bar{2}2)$ is a possible index for point b. By adding $(2\bar{1}\bar{1}0)$ to $(02\bar{2}2)$, a possible index for point c in the diffraction pattern is calculated as $(21\bar{3}2)$. The d-spacing of this plane in the diffraction pattern matches with the d-spacing found in the literature for this planes. The angles between this planes in real space were calculated and compared to the angles between the same planes in the diffraction pattern and correspond to each other within the error margin.

The direction of the electron beam is again the direction perpendicular to all the found planes. The only possible beam direction is the $[0\bar{1}12]$ -direction. This corresponds with an angle of 18.31° with respect c-axis of the hexagonal lattice. So at the location where the diffraction pattern is recorded, the lattice is rotated with an angle of 18° with respect to the lattice in the center of the crystal. However, the axis of rotation at this investigated area inside the crystal differs with around 60° from the axis of rotation on the line between the center and the corner of the crystal, as calculated from the beam-directions. The orientation of the lattice is aligned outwards at this point in the crystal.

3.7 Conclusions

In this chapter, the structure of $\text{Ge}_7\text{Sb}_{93}$ -crystals is investigated. $\text{Ge}_7\text{Sb}_{93}$ -crystals grow in a triangular shape with slightly outwards curved sides. The most important crystal structure of the crystal is the hexagonal lattice, similar to pure antimony lattice, i.e. $R\bar{3}m$ structure. The length of the crystal-axes are changed due to the presence of germanium atoms. The c-axis is slightly bigger compared to the c-axis of the hexagonal lattice of pure Sb while the a-axis is

slightly smaller. With the overall triangular shaped crystal aligned horizontally, the hexagonal lattice in the center of the crystal is oriented with the c -axis vertically, hence with the c -axis pointing upwards.

After a certain distance of growth, the orientation of the crystal in the direction of the corners differs 53° with respect to the center of the crystal. An attempt was made to determine the sign (positive or negative) of this rotation. However, this experiment supplied no answers. To find the direction of this rotation, the experiment has to be done more carefully. By inserting the sample in the TEM-holder in such a way that the in-plane tilting axis is exact perpendicular to the growth direction of the crystal, it should be possible to obtain useful information.

It is also attempted to understand the structure $\text{Ge}_7\text{Sb}_{93}$ -crystals near the center before it reaches the steady value of 53° . However, the lattice besides the line between the center of the crystal and a corner is investigated. It was however possible to see that besides rotation in the direction of the corner, so around the in-plane axis perpendicular to the growth-direction, no other changes occur between the center and the corner of the crystal.

With this investigation about the structure of $\text{Ge}_7\text{Sb}_{93}$ -crystals, the knowledge about the way they grow is expanded. Although this knowledge is not required for present applications containing this material, it might be useful in the future.

Chapter 4. Crystal growth front speed

4.1 Experimental procedure

In this chapter, the crystallization speed of $\text{Ge}_7\text{Sb}_{93}$ is investigated at different temperatures. The goal is to expand figure 2.1 for lower temperatures. This is done by using a heating-holder to insert the $\text{Ge}_7\text{Sb}_{93}$ -sample in the TEM. This heating-holder is capable of heating the sample at a desired temperature with great accuracy. By recording images after a certain time interval, the growth distance as a function of time can be found by measuring the distance to the corner of the crystal from a certain reference point in each of the recorded images. By taking the derivative of the found relations between the position and time, the crystallization speeds can be found.

4.2 Results

Figure 4.1 to figure 4.4 shows the growth of the crystal at 110, 125, 130 and 135° Celsius. As can be seen in figure 3.2, the corners of the crystal can consist of multiple parts. For each of the investigated corners in this section, it is composed of two tips. The growth of both tips are always displayed in the same chart.

Except the ones at 110° Celsius, all sets of data points can be described well by a straight line. The best linear fit is included in the images. In case of 110° Celsius, delaying side-effects seems to play an dominant role in the crystal growth. In figure 4.1, only the stable mid-section is used to make a linear fit. The growth rate of the crystal corners are calculated by taking the derivative with respect to time of the found linear relationships of the growth. Both the tips of the corner should approximately have the same average growth rate after a long time. If one tip starts to lag behind the other one, the growth rate increases if it remains part of the corner. The real crystallization speed can therefore be accurately described as the average of the determined growth rates for both tips of the corner in this relatively short time-range.

The error margin is taken as the difference between the highest growth rate of the fastest corner within the error margins of the individual data points and

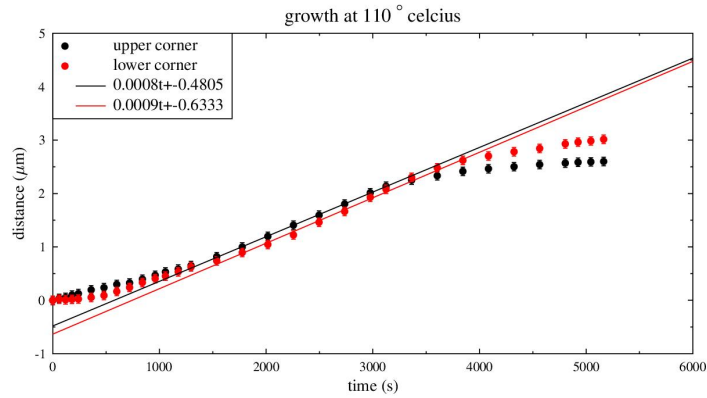


Figure 4.1: The growth of the two parts of a corner of the crystal at a temperature of 110° Celsius.

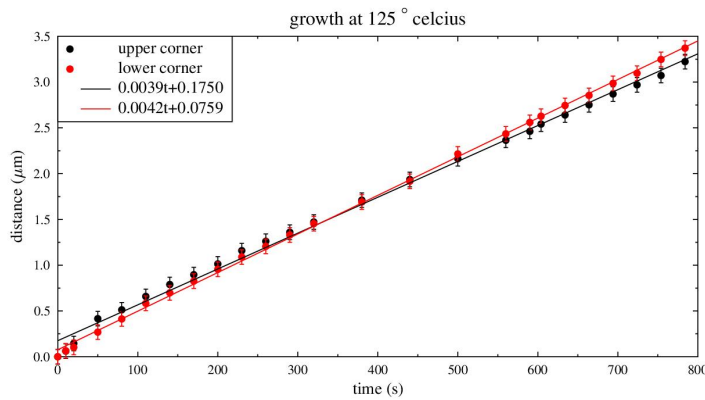


Figure 4.2: The growth of the two parts of a corner of the crystal at a temperature of 125° Celsius.

the lowest growth rate of the slowest corner, again within the error margins of the individual data points. Any possible inaccuracies with defining the tip of the corner are in this way avoided to occur. Table 4.1 shows the calculated average growth rate at different temperatures with their error margins. Due to the nonlinear form of the growth at 110° Celsius, the growth rate found is only valid for the linear mid-section. The error margin of this growth rate is discussed in section 4.4.

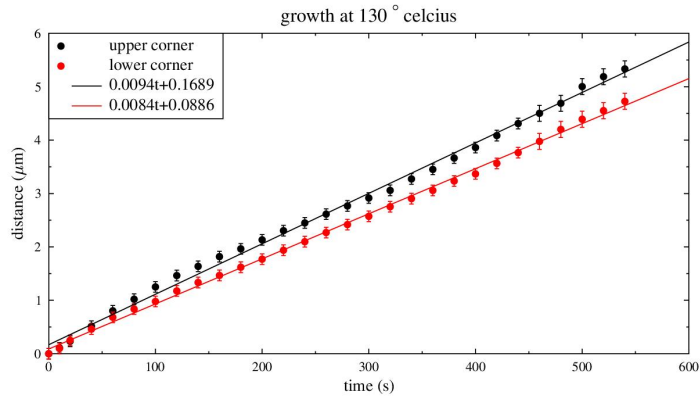


Figure 4.3: The growth of the two parts of a corner of the crystal at a temperature of 130° Celsius.

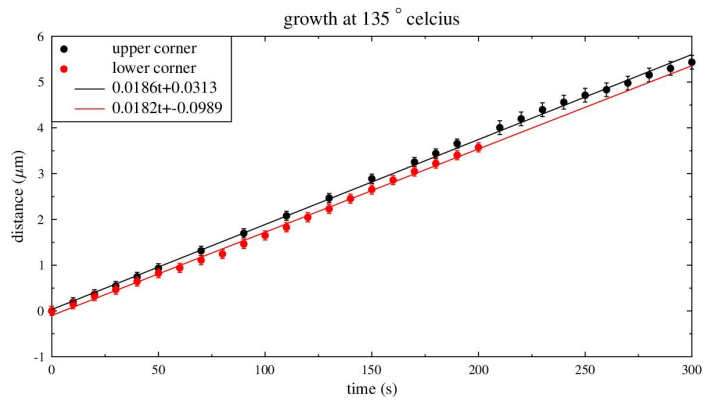


Figure 4.4: The growth of the two parts of a corner of the crystal at a temperature of 135° Celsius.

4.3 Activation energy

The activation energy of a process is defined as the minimum energy required to start the process. Before the germanium-antimony starts to crystallize, a certain amount of energy has to be inserted. Figure 4.5 shows an images which explains this concept.

The value of E_a can easily be calculated by plotting the found values of the growth rate at different temperatures in an Arrhenius plot. An Arrhenius plot is in general a plot of the logarithm of the rate, k , as a function of $1/k_b T$. An

temperature	average growth rate
110 °C	0.0009 $\mu\text{m/s}$
125 °C	0.0041 ± 0.0005 $\mu\text{m/s}$
130 °C	0.0089 ± 0.001 $\mu\text{m/s}$
135 °C	0.0184 ± 0.001 $\mu\text{m/s}$

Table 4.1: The calculated growth rate at different temperatures.

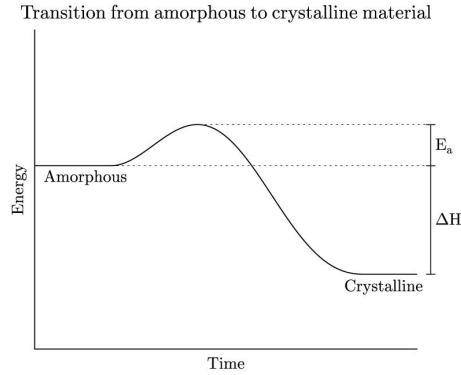


Figure 4.5: The energy level during the transition between amorphous and crystalline material. The value of the activation energy and the change in enthalpy is given in the figure.

example of an Arrhenius plot is already given in figure 2.1. With help of the Arrhenius equation given by

$$k = Ae^{-\frac{E_a}{k_b T}}, \quad (4.1)$$

the activation energy E_a can be calculated. Due to the logarithmic scale of the rate in the Arrhenius plot, the activation energy is proportional to the slope in the plot. Figure 4.6 shows the growth rate for different temperatures of samples covered with different substrates and different thicknesses. As can be seen, both the substrate type and the thickness is of influence on the growth rate. The influence of substrate type can be explained by the thermal expansion coefficients of the used materials in the sample. If the thermal expansion coefficient of the substrate differs from the thermal expansion coefficient of the investigated material, stress occurs when the sample is heated. Previous research has shown that for a certain temperature compressive stress results in a higher growth rate while tension causes a lower growth rate [6]. When the thermal expansion coefficient of the substrate is lower than the thermal expansion coefficient of $\text{Ge}_7\text{Sb}_{93}$, compressive stress arises and the growth rate will go up. It is still unclear how the sample thickness affects the growth rate.

Despite the changed substrate type and thickness dependence of the growth rate, the slope of the lines are reasonable close to each other. This implies

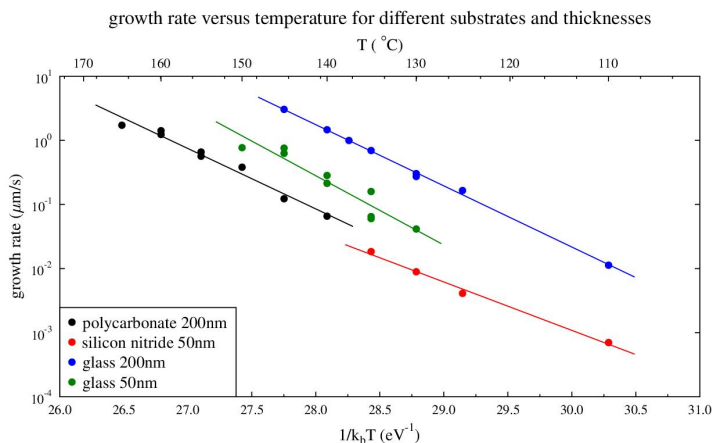


Figure 4.6: The growth rate of $\text{Ge}_7\text{Sb}_{93}$ versus $1/k_b T$ in an Arrhenius plot for samples with different substrates and thicknesses.

that activation energy is almost non-dependent, or completely independent of the substrate type and thickness of the sample. The activation energy for the crystal in the four different samples is given in table 4.2. As can be seen in the

Substrate type and thickness	Activation energy
Silicon nitride 50 nm	2.1057 eV
Polycarbonate 200 nm	2.0682 eV
Glass 200 nm	2.2166 eV
Glass 50 nm	2.5024 eV

Table 4.2: The activation energy for $\text{Ge}_7\text{Sb}_{93}$ in four different samples.

table, the values are reasonable close to each other. The slightly different values might be due to the inaccuracy in the measurements. Figure 4.6 shows that there is deviation of the data points from the calculated best fit, especially for the glass 50 nm- and silicon nitride 50 nm-sample. Hence, there is some error margin to take into account.

4.4 Possible side effects

Beside the dominant effect of the heat produced by the heating holder on the crystallization rate, several side effects play a role in the way the investigated crystal grows. As can be seen in figure 4.1 to figure 4.4, there are effects that have a non-uniform effect in time. This is best seen in figure 4.1, where the growth rate is very low. Up to the middle of the time range, the growth rate increases. In the second half, the growth rate decreases to almost zero. The increasing growth rate starting from $t = 0$ can probably be partly described by

the temperature gradient in the sample. The $\text{Ge}_7\text{Sb}_{93}$ is only heated from the edge of the sample. With the heat transported mainly by the silicon-substrate, it will take some time to reach the desired temperature everywhere in the sample. The decreasing growth rate at the end of the investigated time-range may be due to differences in the crystal structure caused by the electron beam. The long exposure time of the electron beam on the sample caused a black ring at the edge of the viewing area. At the overview images of figure 4.7, it can be seen that the ring acts as a barrier for the crystalgrowth. The circle is almost

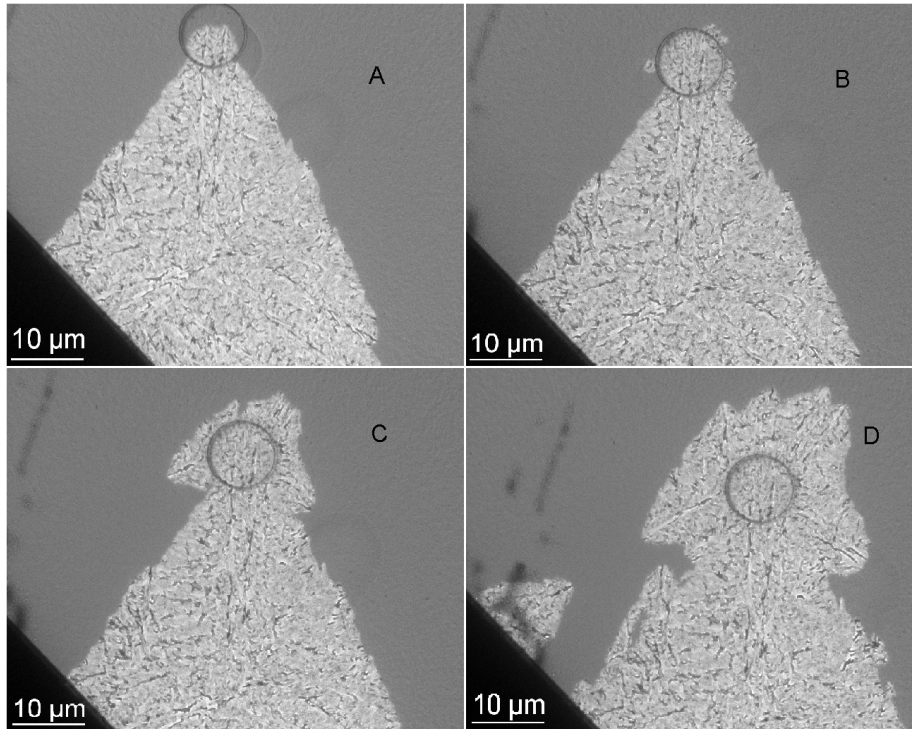


Figure 4.7: An overview of one corner of the crystal after heating at 110° Celsius, A; after heating at 125° Celsius, B; after heating at 130° Celsius, C; after heating at 135° Celsius, D. The visible corner is only irradiated for a long period during the heating at 110° Celsius.

filled completely with crystalline material before it passes the border. Since the other measurements were done on the other corner of the crystal and took significantly less time, this effect is negligible in the results of heating at 125, 130 and 135° Celsius. It is hard to say how large the error margin must be to cover the right value of the growth rate in this case. The slopes of the best fits through the stable mid-section of figure 4.1 are likely the maximum possible values of the growth rate as it would have been without the side-effects. The inhibitory effects seem to have a minimum value in this area while it benefits from the temperature increasing electron beam. The minimum possible value of the growth rate at the temperature of 110° can likely be expressed as the lowest

of the growth rate over the complete time range, $0.0005 \mu\text{m/s}$. The growth rate will then be $0.0007 \pm 0.0002 \mu\text{m/s}$. This argument can be justified by noting that the major part of the growth is dominated by decreasing side effects.

As mentioned before, the electron beam heats the sample. As can be seen in figure 4.7, the crystal grows eventually better from material which is exposed for a long period by the electron beam. Figure 4.7C in particular shows that the only growth occurred arises from the part with the black circle. Only at 135° Celsius, the temperature is high enough to cause visible growth at other places also. This might also be caused by changes in the internal structure due to the electron beam.

At the temperatures of 125, 130 and 135° Celsius some kind of oscillation in the growth rate is visible. This effect is however small compared to the growth rate and will therefore hardly change the error margin. A possible explanation is the non-uniform structure of the crystal. Crystals with a slightly different composition may have different growth rates at a certain temperature. This will cause the oscillatory movement around the linear fits. This effect should obviously also be present at 110° Celsius but it is very small compared to the other side-effects.

4.5 Influence of the electron beam

As discussed before, the electron beam of the TEM affects the results of the experiments. To investigate this disturbance, the growth rate is again measured in the TEM, this time with the electron beam turned off. Because images can not be recorded without the electron beam, this measurements consists only of a couple of measurement-points. After heating for a while, the temperature is set back to room temperature before applying the electron beam. This ensures that the effect of the electron beam is in principle absent or at least minimized. After recording the images, the electron beam is again turned off and the heating mechanism turned on for the next period of heating. The heating time is defined as the time between 1 degree below the desired temperature during the heating and 1 degree below the desired temperature during the cooling. This will ensure a smaller mistake due to growth during the time from room temperature to the desired temperature and the delay between the indicated temperature and temperature inside the sample. Because the earlier used TEM-sample is investigated extensively, a new sample is prepared to be sure that this experiment is not influenced by the prolonged exposure of the electron beam due to previous experiments.

This procedure is used to produce data about the growth at 125, 130 and 135° Celsius. Figure 4.8 shows the obtained data with this experiment. Despite of the low number of measuring points, it is clear from the figure that the growth can be well described by a linear fit for all temperatures.

Figure 4.9 shows the growth rate at different temperatures for both the measurements with and without the electron beam in an Arrhenius plot. As can be seen in the figure, the values are almost equivalent to the ones obtained by

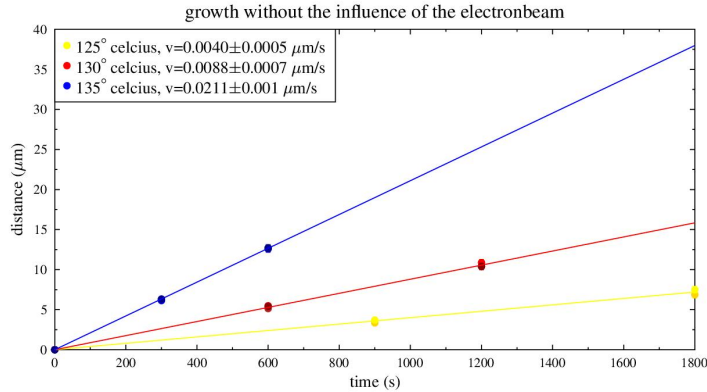


Figure 4.8: The growth of $\text{Ge}_7\text{Sb}_{93}$ at 125, 130 and 135° Celsius measured in the TEM without the influence of the electron beam. The growth rate determined from this data is also given.

measurements with the influence of the electron beam. Only the growth rate at 110° with the influence of the electron beam seems to deviate from the expected value of the growth rate at 110° without the influence of the electron beam. However, growth rate experiments at 110° are too much time consuming for its benefits.

The best fit of the Arrhenius equation through both sets of data points yields the activation energy for both methods. With influence of the electron beam, a lower activation energy is observed. A possible explanation for this phenomenon is the change of the internal structure of the amorphous material. Due to the collisions inside the material with high energetic electrons, the atoms may form some connections with each other which ensures that the structure has become a bit more similar to crystalline structure. As a consequence, the difference in Gibbs free-energy between the amorphous state and the crystalline state is reduced. This will cause easier crystallization of the amorphous structure and may reduce the activation energy [10]. This is exactly what is found after elaboration of the data points from figure 4.9.

4.6 Influence of preheating the material

From previous studies, the presumption is raised that preheating the amorphous material results in higher growth rates. A possible explanation for this phenomenon might again be that the complete amorphous structure changes to a slightly organized amorphous state. After the preheating, less energy would be necessary to crystallize the material. This would result in faster growth rates at certain temperatures.

To test this assumption, the following experiment is devised. The first sample,

Difference between the growth rate obtained with and without the influence of the electronbeam

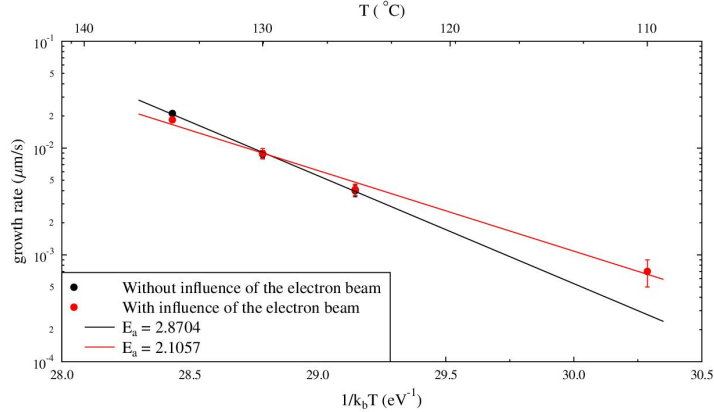


Figure 4.9: The growth rate of $\text{Ge}_7\text{Sb}_{93}$ at different temperatures for measurements with and without influence of the electron beam.

50 nm $\text{Ge}_7\text{Sb}_{93}$ on glass substrate, is heated at 120, 130 and 140° Celsius in that order for a certain amount of time in which the growth rate can be calculated. An identical second sample is heated at 140, 130 and 120° Celsius in that order. By recording images of the crystal with an optical microscope during the growth process, the growth as a function of time can be calculated and therefore the growth rate also. Due to preheating, the growth rate at 140° Celsius in the first sequence should be higher than the growth rate at 140° Celsius in the second sequence. Besides that, the growth rate at 120° Celsius in the second sequence should be higher than the growth rate at 120° Celsius in the first sequence.

The growth rates of both heating-sequences as a function of temperature are given in figure 4.10. The figure shows that the results are different from the expected values. The growth rates of both sample differ at all temperatures approximately a factor two with respect to each other. These results can therefore not be used to say something about the hypothesis.

Because the growth rates for both methods differ consequently a factor two, it is plausible that the indicated temperature at one of the experiments deviates constantly around five degrees more from the actual temperature in the sample than at the other experiment. A possible explanation is that the heating device which is used to heat the sample does not have a uniform temperature. The exact location on the heating device and the shape of the sample might therefore be of influence to the temperature at the investigated area. Also the location of the investigated area on the sample may affect the temperature. The influence of the location on the sample is investigated in the next section.

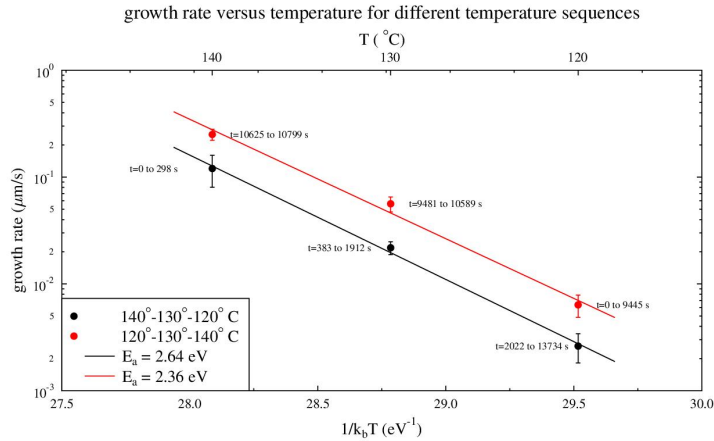


Figure 4.10: The growth rate as a function of temperature for two different heating-sequences. The activation energy and time during the experiment are also given in the graphic.

4.7 Influence of location on the sample

Different locations on a sample might have different temperatures. Close to the edge of the sample, a larger area is in contact with the air. It is expected that these parts are cooler than parts closer to the center of the sample. To examine this hypothesis, a 50 nm $\text{Ge}_7\text{Sb}_{93}$ on glass substrate sample is heated at 130° Celsius. The growth rate is measured at two points simultaneously, very close to the edge and at the center of the sample. This is done by recording images alternately at both places. Table 4.3 gives the measured values of the growth rate. The found values of the growth rate in both cases differ by a factor

Area	Growth rate
Close to the center	$0.0368 \pm 0.007 \mu\text{m/s}$
Close to the edge	$0.0303 \pm 0.007 \mu\text{m/s}$

Table 4.3: The growth rate of $\text{Ge}_7\text{Sb}_{93}$ on glass substrate at different areas of the sample.

1.2. With an activation energy of 2.5 eV, this is equivalent to a temperature difference of around 1 degree Celsius. Although there is a clear difference, it is not enough to completely explain the growth rate difference found of a factor two between two samples in the previous section. Also, because in the previous section there was not such a strong difference in location close to the center and close to the edge as tested here. Probably the difference found in the previous section is really an intrinsic property of crystallization in the amorphous films. More statistics is required to be sure that the effect found in the previous section is really found over and over again.

4.8 Differences in heating the material

So far, two types of heating mechanisms are used to heat the samples to the desired temperatures: The heating stage from the optical setup and the TEM-heating holder. Both mechanisms make use of electrical resistance to produce heat. In both mechanisms, a thermocouple is used to measure the temperature and PID-control is used to reach and maintain the desired temperature. The way heat is transferred to the sample differ from each other. In the optical setup, one of the large area sides of the sample is completely in contact with the heating stage and heat is conducted over the complete sample area only for a short length across the thickness of the substrate. In the TEM-heating holder, only the edge of the sample is heated and heat has to be conducted over the length of the TEM sample. Moreover, heating of the TEM sample has sometime to proceed through thin films, where particularly the Si-nitride windows are poor heat conductors. The second difference is the environment in both cases. Inside the TEM, a vacuum surrounds the sample while the sample in the optical setup is exposed to air.

To determine the differences in growth rate due to heating with the TEM-heating holder and the heating stage of the optical emplacement, the growth rate during the sample-preparations is evaluated. The preparation of both TEM-samples used are performed at 130° Celsius. With both samples, the growth rates at 130° Celsius are also measured with the TEM. Both heating mechanisms can therefore be compared to each other. Also, the consistency of the result can be examined.

Table 4.4 shows the relevant growth rates for comparing both heating mechanisms.

50 nm Ge₇Sb₉₃ on silicon nitride substrate (sample a)			
Temperature	Measurement method	Details	Growth rate
130° C	optical	-	0.096 ± 0.02 μm/s
130° C	TEM	influence of beam	0.0089 ± 0.0010 μm/s
50 nm Ge₇Sb₉₃ on silicon nitride substrate (sample b)			
Temperature	Measurement method	Details	Growth rate
130° C	optical	-	0.0906 ± 0.009 μm/s
130° C	TEM	no influence of beam	0.0088 ± 0.0007 μm/s

Table 4.4: The growth rate at 130° Celsius measured with the TEM and the optical emplacement.

As can be seen in the table, the growth rate measured with the optical setup is for both cases approximately 10 times higher than the growth rate measured with the TEM. The most obvious explanation is that the actual temperature inside the sample in the optical setup is higher than the temperature inside the sample in the TEM. By extrapolating the lines in figure 4.9, the temperature must be set approximately 15° Celsius higher in the TEM to reach equal growth rates. Assuming that the thermocouples in both mechanisms are calibrated well,

the cause of the temperature discrepancy should be searched in the differences discussed before.

The heat transfer to the sample of the heating stage of the optical setup is more advantageous than the method used in the TEM-heating holder. A larger area is used to convey the heat to the sample. With the TEM-heating holder, it is likely that there exist a temperature gradient in the sample. The temperature at the edge is probably higher than at the center. While the TEM measurements are done close to the center of the sample, the temperature measurements took place at the edge. The actual temperature is therefore lower than the set temperature due to energy-loss.

In both mechanisms, the actual temperature will be lower than the set temperature because the loss of energy. Because of the vacuum in the TEM, the only possible way of losing energy is by radiation. Because the sample is besides the heating device not touching anything, conduction or convection of energy is not an issue. This is different for the optical setup. Besides radiation, the sample will also lose energy by conduction and in particular convection due to the air surrounding the sample.

4.9 Conclusions

In-situ heating in the TEM is very useful to find the growth rates at different temperatures of $\text{Ge}_7\text{Sb}_{93}$. The relation between the growth rate and the temperature is found to be follow the Arrhenius equation. Using the Arrhenius equation, it is also determined that the activation energy for growth of the used 50nm thick $\text{Ge}_7\text{Sb}_{93}$ -sample with a Silicon-nitride substrate is equal to $\text{Ge}_7\text{Sb}_{93}$ -samples with a different thickness and substrate-type. However, the growth rate at a certain temperature does depend on the thickness and the substrate-type of the sample.

It is expected that the electron beam of the TEM influences the crystal growth rates in the sample. The high-energetic electrons react with the amorphous structure to order the atoms in a slightly crystallized form. It was predicted that this change in structure would increase the growth rate at a certain temperature. However, experiments on the growth rate with and without the influence of the electron beam showed that the change in internal structure caused no clear change in the growth rate.

An optical setup to measure the growth rates at various temperatures showed an increase of a factor 10 with respect to the TEM-experiments on the growth rate at the same temperatures. This is in accordance with a temperature of around 15° lower than indicated for the TEM than for the optical setup. It is investigated if the location on the samples where the experiments are performed is of influence of the result. With the optical setup however, the most extreme difference in location on the sample resulted in a temperature difference of at most 1° . Also pre-heating the sample is investigated as a possible cause of large differences between both experimental setups but also this did not supplied answers. The presumption is raised that the differences are caused by the way the

samples are connected with the heating devices inside both setups. Also the calibration of both devices might be of influence. Calibration experiments on both the TEM and the optical setup must reveal the real temperature in both setups. However, it is expected that in the TEM the actual thin area analyzed has a lower temperature than that given by the thermocouple connected to the furnace of the TEM heating holder. In this respect the 15° discrepancy can be probably explained.

Chapter 5. Acknowledgments

The author is grateful for the help of Prof. Dr. ir. B.J. Kooi during the entire project, the help of ing. G. Ten Brink concerning ICT- and TEM-issues, and ir. G. Eising for help with the optical setup.

Bibliography

- [1] JONES and AKOLA, *Jülich Scientific Report* **2009**, 64 (2009).
- [2] L. VAN PIETERSON, M. LANKHORST, M. VAN SCHIJNDEL, A. KUIPER, and J. ROOSEN, *Journal of Applied Physics* **97**, 083520 (2005).
- [3] D. ADELERHOF, *E*PCOS* (2004).
- [4] R. PANDIAN, *Phase-change thin films: Resistance switching and isothermal crystallization studies*, (Groningen University Press, Groningen, 2008).
- [5] G. SAKR, *Journal of Electronic Materials* **41**, 2399 (2012).
- [6] G. EISING and B. KOOI, Crystal growth in Ge-Sb compositions and the influence of stresses, in *M2i internal report (M62.7.08SDMP03 - 2012 Q4 Eising)*.
- [7] D. SHAKHVOROSTOV, R. A. NISTOR, L. KRUSIN-ELBAUM, G. J. MARTYNA, D. M. NEWNS, B. G. ELMEGREEN, X. LIU, Z. E. HUGHES, S. PAUL, C. C. JR., S. RAOUX, D. B. SHREKENHAMER, D. N. BASOV, Y. SONG, and M. H. MÜSER, *Applied Physical Sciences* **106**, 10907 (2009).
- [8] H. TASHIRO, M. HARIGAYA, K. ITO, M. SHINKAI, K. TANI, N. YIWATA, A. WATADA, N. TOYOSHIMA, K. MAGITA, A. KITANO, and K. KATO, *E*PCOS* (2003).
- [9] D. B. WILLIAMS and C. B. CARTER, *Transmission Electron Microscopy*, (Springer, New York, 1996).
- [10] R. PANDIAN, B. KOOI, J. D. HOSSON, and A. PAUZA, *Journal of Applied Physics* **101**, 053529 (2007).
- [11] W. D. CALLISTER and D. G. RETHWISCH, *Materials Science and Engineering*, (WILEY, Singapore, 2011).

Chapter 6. Appendices

6.1 All measured growth rates

50 nm Ge ₇ Sb ₉₃ on silicon nitride substrate (sample a)			
Temperature	Measurement method	Details	Growth rate
130° C	optical	-	0.096 ± 0.02 μm/s
110° C	TEM	influence of beam	0.0007 ± 0.0002 μm/s
125° C	TEM	influence of beam	0.0041 ± 0.0005 μm/s
130° C	TEM	influence of beam	0.0089 ± 0.0010 μm/s
135° C	TEM	influence of beam	0.0184 ± 0.0010 μm/s
50 nm Ge ₇ Sb ₉₃ on silicon nitride substrate (sample b)			
Temperature	Measurement method	Details	Growth rate
130° C	optical	-	0.0906 ± 0.009 μm/s
120° C	TEM	influence of beam	0.0045 ± 0.0008 μm/s
130° C	TEM	no influence of beam	0.0088 ± 0.0007 μm/s
135° C	TEM	no influence of beam	0.0211 ± 0.001 μm/s
125° C	TEM	no influence of beam	0.0040 ± 0.0005 μm/s
50 nm Ge ₇ Sb ₉₃ on glass substrate (sample c)			
Temperature	Measurement method	Details	Growth rate
140° C	optical	-	0.120 ± 0.04 μm/s
130° C	optical	-	0.0218 ± 0.003 μm/s
120° C	optical	-	0.00262 ± 0.0008 μm/s
50 nm Ge ₇ Sb ₉₃ on glass substrate (sample d)			
Temperature	Measurement method	Details	Growth rate
120° C	optical	-	0.00636 ± 0.0015 μm/s
130° C	optical	-	0.0563 ± 0.009 μm/s
140° C	optical	-	0.251 ± 0.03 μm/s
50 nm Ge ₇ Sb ₉₃ on glass substrate (sample e)			
Temperature	Measurement method	Details	Growth rate
130° C	optical	center of sample	0.0368 ± 0.007 μm/s
130° C	optical	edge of sample	0.0303 ± 0.007 μm/s

Table 6.1: All growth rate investigations on five different samples in chronological order.

6.2 Vegard's law

The lattice parameters of a binary system can be approximated by Vegard's law:

$$a_{AB} = xa_A + (1 - x)a_B, \quad (6.1)$$

with a_{AB} the lattice parameter a for the combined system and x the fraction of A-atoms. This law however, is in particular only useful for metal compounds due to their preference to form close packed structures. Determined values with help of Vegard's law concerning germanium can therefore, due to the covalent bonds with germanium, not be considered as correct. However, it might possible to use the law for finding a rough estimate of the lattice parameters of the combined GeSb system.

Because of the diamond-structure of the Ge-lattice, Vegard's law cannot be used in the form given by equation 6.1. The nearest neighbor distances of both Ge and Sb atoms are used to determine the nearest neighbor distance of the crystal structure in the combined system. The nearest neighbor distance of Ge atoms in diamond-structure is equal to

$$(2r)_{Ge} = \frac{1}{4}\sqrt{3} \cdot a_{Ge} = 2.450\text{\AA}. \quad (6.2)$$

The nearest neighbor distance of Sb is just

$$(2r)_{Sb} = a_{Sb} = 4.307\text{\AA}. \quad (6.3)$$

According to Vegard's law the approximate nearest neighbor distance for the combined system, and so the a-axis of its hexagonal-lattice, is given by

$$a_{Ge_7Sb_{93}} = (2r)_{Ge_7Sb_{93}} = 0.07(2r)_{Ge} + (1 - 0.07)(2r)_{Sb} = 4.177\text{\AA}. \quad (6.4)$$

The factor

$$f = \frac{(2r)_{Ge_7Sb_{93}}}{(2r)_{Sb}} = \frac{4.177}{4.307} = 0.970 \quad (6.5)$$

can be used to find the length of the c-axis:

$$c_{Ge_7Sb_{93}} = c_{Sb} * f = 11.273 * 0.970 = 10.935\text{\AA}. \quad (6.6)$$

These results are different from the experimentally found values mentioned in section 2.3. The a-axis as well as the c-axis are 3% smaller in Ge₇Sb₉₃ compared to pure Sb, as determined with Vegard's law. Experiments reveal however that the a-axis is around 0.2% smaller while the c-axis is around 0.2% bigger in Ge₇Sb₉₃ compared to pure Sb. With this, it is made clear that Vegard's law is invalid for the GeSb-system.

6.3 Vectors in the Miller-Bravais index system

Different from planes, the conversion of vectors between the three indices from the Miller-index system and the four indices from the Miller-Bravais-index system is not obvious. The conversion of vectors to the Miller-Bravais-index system is accomplished by working out the formulas

$$a_1 = \frac{1}{3}(2a'_1 - a'_2), \quad (6.7)$$

$$a_2 = \frac{1}{3}(2a'_2 - a'_1), \quad (6.8)$$

$$a_3 = -(a_1 + a_2), \quad (6.9)$$

and

$$a_4 = a'_4 [11]. \quad (6.10)$$

The primed indices in this formulas are part of the Miller-index system while the unprimed indices are part of the Miller-Bravais-index system. With the indices known, the vector can be constructed inside a hexagonal unit cell by adding each component to each other in the right direction starting from a certain point inside the lattice, as one would also do with a normal vector in a cubic space-system, or can directly be converted to a vector in a cubic system. The conversion to the cartesian coordinate system can be done by working out the formula

$$\vec{x} = \begin{pmatrix} \frac{1}{2}a(a_1 + a_2 - 2a_3) \\ \frac{\sqrt{3}}{2}a(a_2 - a_1) \\ c * a_4 \end{pmatrix}, \quad (6.11)$$

where the direction of all the used axes are given in figure 6.1. a en c in this formula are the lengths of the axes which define the size of the hexagonal lattice, as usual. A constructed vector in Miller-Bravais indices will be exactly the same

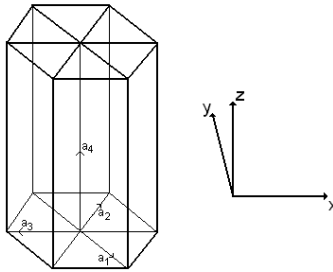


Figure 6.1: The definition of the direction of the used axes in this section.

as a vector that can be constructed by adding each component of the Miller-index system to each other in the same way.